UC Berkeley

Title

Development of an efficient immersed-boundary method with subgrid-scale models for conjugate heat transfer analysis using large eddy simulation

Permalink

https://escholarship.org/uc/item/1st51860

Authors

Lee, Sangjoon
Hwang, Wontae

Publication Date

DOI

Copyright Information

Peer reviewed

Development of an Efficient Immersed-Boundary Method with Subgrid-Scale Models for Conjugate Heat Transfer Analysis using Large Eddy Simulation

Sangjoon Lee[a], Wontae Hwang[a,b,*]

[a]*Dept. of Mechanical and Aerospace Engineering, Seoul National University, 1 Gwanak-Ro, Gwanak-Gu, 08826, Seoul, Republic of Korea*
[b]*Institute of Advanced Machines and Design, Seoul National University, 1 Gwanak-Ro, Gwanak-Gu, 08826, Seoul, Republic of Korea*

Abstract

A numerical procedure for conjugate heat transfer (CHT) analysis based on an immersed boundary (IB) method for large eddy simulation (LES) has been developed. The dynamic subgrid-scale (SGS) stress and heat flux models are implemented in the solver. Since discrepancy between the computational grid and solid-fluid interface generally exists, interpolation of thermal properties at the interface is necessary for the current method. Accordingly, an efficient interpolation scheme using the modified flood-fill algorithm is applied. In order to validate the capability of the developed method, three different CHT cases with turbulent flow were examined: channel flow between heated slabs, thermally-driven flow in a closed cavity, and crossflow around a heated circular cylinder. Compared to cases that just utilized an isothermal or constant-heat-flux boundary condition, when the CHT method was properly implemented, results more closely matched experimental data and existing correlations.

Keywords: Conjugate heat transfer analysis, Large eddy simulation, Subgrid-scale model, Immersed boundary method, Solid-fluid interface interpolation

1. Introduction

Many systems are analyzed assuming convection is the principal mode of heat transfer, such as gas turbines, heat exchangers, and heating, ventilation and air conditioning (HVAC) systems. Heat conduction is often ignored or ideally modelled during the analysis. However, conduction inside solid walls is often important. When this is not properly considered, a major issue arises in that the thermal boundary condition of the solid-fluid interface remains unknown.

Accordingly, many previous studies conducting heat transfer analysis dealt with this issue by assuming the interface has as an isothermal or constant heat flux boundary condition [1–6], or utilizing the data reduction technique via the thermal resistance concept [7, 8]. Some of these studies seemed to have reasonable success when compared against experimental data [1, 7].

Nevertheless, these assumptions do not reflect the actual physics at the solid-fluid interface, resulting in a disparity of results compared to experiments. For example, in the tubular-type heat exchanger study of Castro et al. [5], which applied constant wall temperature boundary conditions, the results of the numerical simulations showed 15% error compared to measurements. Furthermore, Jayakumar et al. [6] examined a heat exchanger with a helical coil, and found that the use of isothermal or constant heat flux boundary conditions for such a system does not yield proper results. They claimed that conjugate heat transfer (CHT) analysis is essential for modeling.

CHT considers both heat conduction in the solid and heat convection in the fluid simultaneously, and thus fundamentally resolves the shortcoming stated above. As Bohn et al. [9] indicated, CHT does not employ arbitrary thermal boundary conditions at the solid-fluid interface. CHT also physically models the conduction process, thus giving more reasonable heat transfer results. For example, Webb and Ramadhyani [10] investigated a channel flow with staggered ribs through CHT, and showed that conduction in the wall and ribs played a highly favorable role in improving heat transfer. Oda et al. [11] utilized CHT in pin-fin channels to assess heat transfer from the pin-fin surfaces.

In CHT, there are two main procedures for treating the solid and fluid domains. One is domain decomposition [12, 13]. This procedure separates the solid and fluid region during calculation, and then sets the interface values to match the boundary conditions. Although accuracy is good, the domain decomposition procedure requires extra iterations for interface matching, and thus takes longer to converge. To overcome these shortcomings, some researchers selected another procedure that treats both regions as a unitary computational domain [14, 15]. The approach enforces the velocity inside the solid domain to be zero and satisfies thermal continuity at the solid-fluid interface.

The immersed boundary (IB) method is one of the practical CHT approaches that uses a unitary computational domain. Iaccarino and Moreau [16] extended their incompressible Reynolds-averaged Navier-Stokes (RANS) solver with IB to include CHT in a Cartesian grid system, and verified its capability on convection flows in complex geometries. Nagendra et al. [17] suggested a new CHT-IB approach for curvilinear grid based solvers, using an efficient search-locate and interpolate

algorithm. Song et al. [18] proposed a CHT-IB method using two additional non-dimensional values, a thermal conductivity ratio of solid to fluid K, and a volumetric heat capacity ratio of fluid to solid C.

In the present work, a new CHT-IB method with subgrid-scale (SGS) models for use in a Cartesian grid system is developed for large eddy simulation (LES). The LES solver includes a SGS stress model for the momentum equation and SGS heat flux model for the energy equation. The solver enables the code to analyze turbulent flow in complex geometries more accurately than RANS, and more economically than direct numerical simulation (DNS). Since the solid-fluid interfaces embodied by IBs do not coincide with the grids in general, an additional interpolation step is required for the interface cells. The interpolation method of thermal properties at solid-fluid interfaces and the procedure for implementing the efficient weighted-average algorithm will be discussed. In order to validate the capability of the code, three different turbulent flow problems were simulated and compared with previous studies, including an internal channel flow, a circulating flow in a closed cavity, and an external crossflow around a circular cylinder.

2. CHT-IB method with SGS models

2.1. Governing equations

In this study, the grid-filtered incompressible Navier-Stokes equation and the grid-filtered thermal energy equation are used as governing equations. In the dimensionless form, the continuity, momentum, and thermal energy equations are expressed as

$$\frac{\partial \overline{u_i}}{\partial x_i^*} - m = 0 \tag{1}$$

$$\frac{\partial \overline{u_i}}{\partial t^*} + \frac{\partial \overline{u_i}\,\overline{u_j}}{\partial x_j^*} = -\frac{\partial \overline{p}}{\partial x_i^*} + \frac{1}{Re}\frac{\partial^2 \overline{u_i}}{\partial x_j^* \partial x_j^*} + \frac{Gr\overline{\theta}}{Re^2} - \frac{\partial \tau_{ij}}{\partial x_j^*} + f_i \tag{2}$$

$$\frac{\partial \overline{\theta}}{\partial t^*} + \omega \frac{\partial \overline{u_i}\,\overline{\theta}}{\partial x_i^*} = \frac{C^* K^*}{RePr}\frac{\partial^2 \overline{\theta}}{\partial x_i^* \partial x_i^*} - \frac{\partial \varphi_i}{\partial x_i^*} + \zeta \tag{3}$$

where x_i^* are the Cartesian coordinates, t^* is the time, u_i are the velocity components, m is a mass source/sink, p is the pressure, θ is the temperature, τ_{ij} is the SGS stress, f_i is a momentum forcing term, ω is a correction factor, K^* is the thermal conductivity ratio, C^* is the volumetric heat capacity ratio, φ_i is the SGS heat flux, and ζ is a heat source/sink. It should be noted that all of these variables are non-dimensional. Re, Pr, Gr are Reynolds, Prandtl, and Grashof numbers, respectively. The existence of Gr in Equation (2) extends the method's usage to natural or mixed convection problems, such as gas turbine casing flows during engine shutdown [19].

Overbars on u_i, p, and θ mean that each physical property is a grid-filtered value, resulting in the generation of SGS stress τ_{ij} and heat flux φ_i in the equations:

$$\tau_{ij} = \overline{u_i u_j} - \overline{u_i}\,\overline{u_j} \tag{4}$$

$$\varphi_i = \overline{u_i \theta} - \overline{u_i}\,\overline{\theta} \tag{5}$$

Since the product of unfiltered variables are unknown in Equation (4) and (5), SGS models are implemented to obtain the SGS terms. To calculate the SGS stress term, the dynamic model with global coefficients based on the Germano identity suggested by Park et al. [20] is applied. Unlike the earlier work of Smagorinsky [21], the model utilizes the SGS eddy viscosity model of Vreman [22], such that the SGS eddy viscosity normally vanishes at the region where the SGS dissipation is theoretically zero, thus increasing the accuracy. In the case of the SGS heat flux term, the dynamic linear eddy diffusivity model proposed by Moin et al. [23] is used. The model's linear constitutive relation has been sometimes regarded as overly simplified, but has successfully predicted various thermal convective flows [24]. Instead of applying the SGS heat flux model, some previous studies adopted a constant ratio of the eddy viscosity and the eddy diffusivity, or turbulent Prandtl number (Pr_T), thus indirectly obtaining the eddy diffusivity from the eddy viscosity calculated from the SGS stress model [25–27]. Since there is no suitable physical background for the constant Pr_T, however, this approach is not exploited in the present study.

Based on the IB method, solid-fluid interfaces are specified by introducing a mass source/sink m into the continuity equation and momentum forcing f_i into the momentum equation. The details of deciding both terms are explained in Kim et al. [28]. After implementation, all velocity components inside the solid body and at the solid-fluid interfaces become nulled.

In order to treat both heat conduction and heat convection in the single thermal energy equation, the correction factor ω and thermal conductivity and volumetric heat capacity ratios K^* ($= k_{cell}/k_f$) and C^* ($= (\rho c_p)_f / (\rho c_p)_{cell}$), suggested by Song et al. [18], are added. ω is zero in the cells containing solid, and unity in the others. K^* and C^* can be simply determined for pure fluid or solid cells. At the interface cells, however, these values vary with the fluid-solid configuration of each cell, which will be further described in Section 2.2. A general CHT-IB domain is illustrated in Fig. 1.

2.2. Interpolation of thermal properties at solid-fluid interfaces

One of the main issues of the IB method is the discrepancy between the solid-fluid interfaces and the computational grid, which inevitably generates interface cells which contain both fluid and solid regions. In order to satisfy the continuity of temperature and the conservation of thermal energy, a plausible interpolation scheme for the CHT coefficients at each interface cell is necessary. The interpolation is also needed to make the LES results using the SGS models more reliable, because it plays a key role in defining the exact geometry during calculation. If the geometry is poorly given, the results would be unreliable even though the LES itself well resolves turbulent properties. In the case of the volumetric heat capacity, it seems reasonable that the weighted volume average over the cell can serve as the interpolated value. Provided that the volumetric proportion of fluid in an arbitrary interface cell is ε ($0 < \varepsilon < 1$), the nominal volumetric heat capacity at the cell is given as:
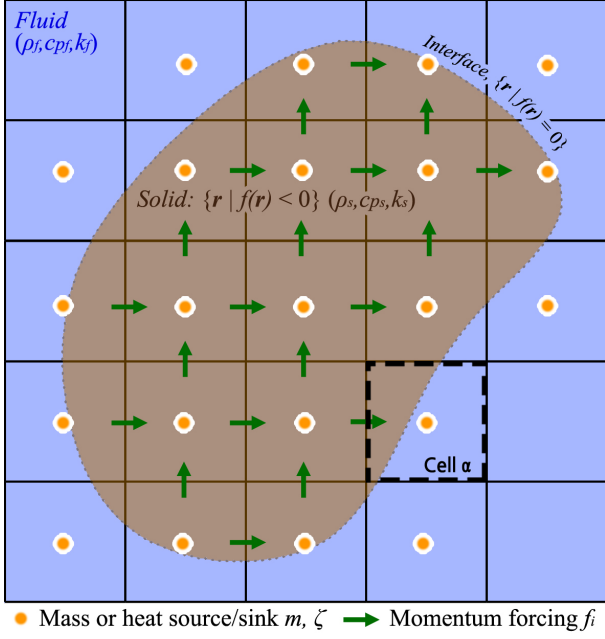
Fig. 1. Schematic diagram of a general CHT-IB domain. The predetermined function f specifies the Lagrangian solid body in the Eulerian flow field. CHT coefficients are interpolated at interface cells, like Cell α within the dashed line.

$$\left(\rho c_p\right)_{cell} = \varepsilon\left(\rho c_p\right)_f + (1 - \varepsilon)\left(\rho c_p\right)_s \qquad (6)$$

The thermal conductivity, unlike the heat capacity, should be determined at each face of the interface cell because the heat flux comes across it. The basic concept with details is introduced in Song et al. [18]. As depicted in Fig. 2, to obtain the thermal conductivity at the left face of the interface cell (denoted as the black box), an interim cell denoted as the blue dashed box is utilized to calculate the volume averaged thermal conductivity, which would be closer to that of a solid in this case. This would be a more accurate representation for this face, than to use the same volume averaged conductivity for all faces of the interface cell. In the same manner, interim cells are utilized to calculate the conductivity for all faces of the interface cell.

Next, we assume that the volumetric proportion of fluid in the corresponding interim cell is ψ ($0 < \psi < 1$). If the phase at the cell center changes for the adjacent cell, a harmonic weighted volume average is applied to determine the nominal thermal conductivity:

$$k_{cell} = \frac{k_s k_f}{k_s \psi + k_f(1 - \psi)} \qquad (7)$$

If it does not change, a simple weighted volume average is used instead:

$$k_{cell} = \psi k_f + (1 - \psi) k_s \qquad (8)$$

Since it is time-consuming to calculate these proportions one by one, an efficient algorithm needs to be utilized for the interpolation scheme. In this study, a modified flood-fill algorithm
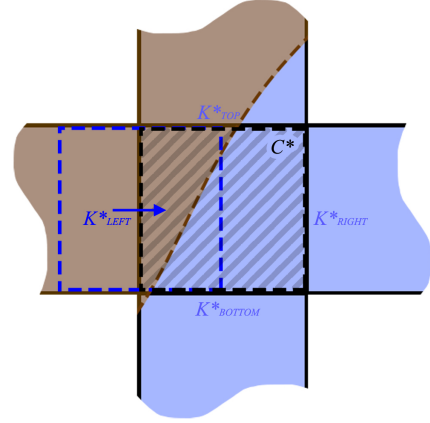

Fig. 2. An interface cell and its neighboring cells providing or receiving heat flux

has been devised, which subdivides the cell at regular intervals and recursively finds sub-cells whose center is in the fluid phase. The steps of the algorithm are presented in Fig. 3. At the beginning, the sub-cell located at one corner is identified as fluid or solid. Next, the sub-cell triggers the same identification process at the adjacent sub-cells which are not identified yet. The process stops when the adjacent sub-cell is outside of the main cell (as can be seen with the 'O' in Fig. 3), or the phase of the sub-cell changes (as can be seen with the 'S' in Fig. 3). The algorithm terminates when no more process calls remain in the stack.

It should be noted that unidentified sub-cells might exist, as shown in Fig. 3 for the one marked with an 'A'. However, the phase of these sub-cells can be automatically regarded as opposite to that of the first identified sub-cell, under the assumption that only a single solid-fluid interface per cell exists. This assumption should hold because it is also a prerequisite for an acceptable grid condition near the wall for the IB method. Since these unidentified sub-cells are not involved in the recursion process, they essentially decrease the computational time.

When the number of subdivision levels increases, a more accurate proportion of fluid can be obtained, likely resulting in more accurate CHT results. However, the computational time also rapidly rises, in the order of number of subdivision levels cubed. This becomes more critical for moving IB problems because the interpolation algorithm needs to be executed at the refreshed solid-fluid interfaces for every timestep. Therefore, it
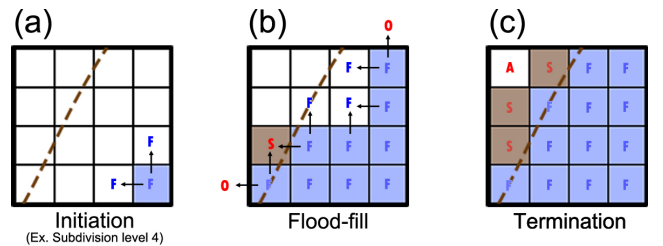

Fig. 3. Steps of the modified flood-fill algorithm for the interpolation. (a) Initiation stage, (b) interim stage, and (c) termination stage.

is important to find the optimal level of subdivision considering this trade-off between accuracy and computational time. The optimization process will be further discussed with the code validation in Section 3.3.

2.3. General procedures

The overall numerical scheme and the determination of the IB terms are based on the finite volume method of Kim et al. [28, 29]. These procedures use a second-order central difference method for space and a semi-implicit fractional-step method for time (a 3rd-order Runge-Kutta scheme for convective terms and the Crank-Nicolson scheme for diffusive terms). For the calculation of CHT coefficients, the modified flood-fill algorithm in Section 2.2 is applied with various subdivision levels, in order to find the optimum fluid proportion. Finally, the SGS terms for LES are derived from the dynamic SGS eddy viscosity and diffusivity models. In both of the SGS models, the model coefficients are dynamically determined via the least-square technique proposed by Lilly [30]. To ensure the convergence of the numerical solution, the interval of each timestep is restricted by the Courant-Friedrichs-Lewy (CFL) condition. The maximum CFL number is identically set to unity.

Most modules that requires intensive arithmetic, including the main solver, are written in Fortran 90. All other modules are written in Python 3. The code was executed through a single personal computer with 64 GB memory, which shows 274 GFLOPS at full CPU performance using 10 parallel cores.

3. Code validation and results

For the purpose of validating the current CHT-IB method for LES, three different turbulent flow cases were modelled and simulated, as shown in Table 1. The following points were investigated to confirm the code's performance. First, the differences between CHT and non-CHT analyses were examined in heated channel flow. Next, the capability of predicting thermally-driven free convection was verified through closed cavity flow. Lastly, the optimal level of subdivision for the interpolation scheme will be discussed with crossflow around a heated cylindrical body.

3.1. Channel flow between two heated slabs

Turbulent channel flow between two heated parallel slabs (see Fig. 4) was simulated and compared with the direct numerical simulation (DNS) data of Tiselj et al. [31]. For this case, two slabs containing a constant volumetric heat source (q) heat the system, whose outer boundaries are assumed to be adiabatic. The reference length, velocity, and temperature for the nondimensionalization were chosen as the channel height 2, bulk velocity U_b, and the scaling temperature $\xi\delta/[U_b(\rho c_p)_f]$. The grid parameters and material properties are listed in Table 2. $Re = 4,620$ is selected to correspond to $Re_\tau = 150$ [32]. Temperature is assumed to be a passive scalar, and therefore buoyancy is neglected ($Gr = 0$).

In this case, the temperature linearly rises with respect to x even after the flow becomes fully developed. According to

Kawamura et al. [33], the dimensionless temperature can be decomposed into two parts: $\theta = (\mathrm{d}\langle\theta\rangle/(\mathrm{d}x^*))x^* - \widetilde{\theta}$, where $\langle\theta\rangle$ is defined as

$$\langle\theta\rangle = \int_0^1 u_x\theta\mathrm{d}y^* \bigg/ \int_0^1 u_x\mathrm{d}y^* \tag{9}$$

and $\widetilde{\theta}$ is the residual non-dimensional temperature. Assuming fully developed conditions, the $\langle\theta\rangle$ streamwise gradient becomes 2, thus $\theta = 2x^* - \widetilde{\theta}$. Using this transformation, the energy equation for the fluid can be written as

$$\frac{\partial\widetilde{\theta}}{\partial t^*} + \frac{\partial u_i\widetilde{\theta}}{\partial x_i^*} = \frac{1}{RePr}\frac{\partial^2\widetilde{\theta}}{\partial x_i^*\partial x_i^*} + 2u_x \tag{10}$$

The above equation is then grid-filtered and discretized for this case, and thus $\widetilde{\theta}$ is calculated instead of θ. For convenience, the tilde superscript (˜) will be omitted hereinafter.

For the boundary conditions, a no-slip condition is applied at the solid-fluid interface, and periodic boundary conditions maintaining uniform system enthalpy and volumetric flow rate are imposed in the streamwise (x) and spanwise (z) directions. The slab outer boundaries are adiabatic, and thu s represented as $\partial\theta/\partial y^* = 0$.

The initial flow field is defined as a uniform velocity profile, with superposition of random velocity perturbations ranging up to $0.1U_b$. The initial θ for all cells is set to zero. Next, in order to obtain fully developed flow, simulations are carried out for the time interval of $1500\delta/U_b$ without averaging, which is sufficiently longer than that of Tiselj et al. [31]. After both velocity and temperature fields are fully developed, additional calculations for the time interval of $1500\delta/U_b$ are performed to obtain turbulent statistics.

Grid dependency was checked, and the results are in Table 3. The medium grid size is sufficient for estimating mean properties, showing less than 2% absolute error for friction factor and mean non-dimensional temperature θ_m at the centerline. For fluctuating properties, however, the fine grid size is recommended, considering the steep sensitivity of the error of θ_{RMS} at the wall. Thus, the fine grid system is selected for further simulations hereinafter. It is additionally noted that the friction
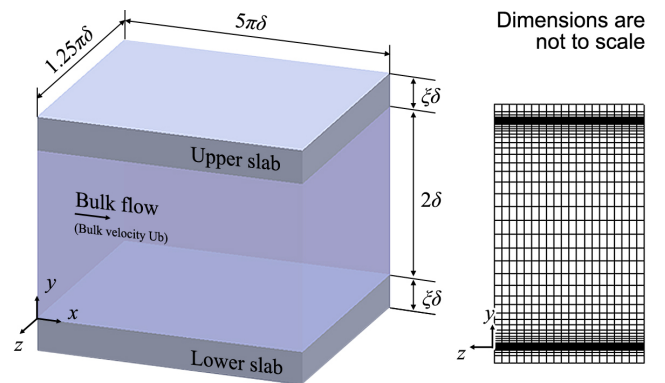

Fig. 4. (Left) geometry of channel flow between two heated parallel slabs and (right) grid system viewed at *yz*-plane.

4

Table 1
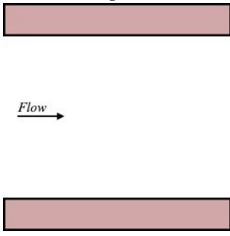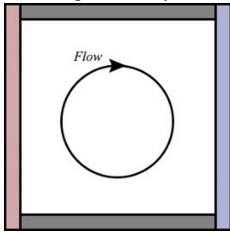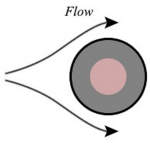Overview of three validation cases

Case Name	Channel flow between two heated parallel slabs	Free convection in a closed square cavity	Crossflow around a heated circular cylinder
Geometry	*Flow* →	*Flow*	*Flow*
Flow type	Internal flow with bulk movement	Internal flow without bulk movement	External flow
Convection type	Forced convection	Free convection	Forced convection
Temperature field	Passive scalar	Active scalar	Passive scalar
Solid-fluid interface	Rectilinear	Rectilinear	Curvilinear
Grid-interface discrepancy	No	No	Yes

Table 2
Grid parameters and material properties for channel flow

Domain size, $L_x \times L_y \times L_z$		$5\pi\delta \times 2(1 + \xi)\delta \times 1.25\pi\delta$		
Grid type		Coarse	Medium	Fine
Cell arrangement, $N_x \times N_y \times N_z$		$40 \times 64 \times 20$	$60 \times 96 \times 30$	$120 \times 160 \times 60$
Total number of cells		51,200	172,800	1,152,000
Grid interval (wall units)*	Δx^+	58.9	39.3	19.6
	Δy^+	0.2 - 18.2	0.2 - 11.0	0.1 - 9.2
	Δz^+	29.5	19.6	9.8
Number of cells inside the slab in the y-direction		7	10	32
Reynolds number, *Re*		4,620		
Prandtl number, *Pr*		7		
Slab thickness (wall units)*, $(\xi\delta)^+$		20		

* Wall unit values here are calculated at $Re_\tau = 150$.

Table 3
Grid dependency test for channel flow. The errors are based on the DNS values [31, 32].

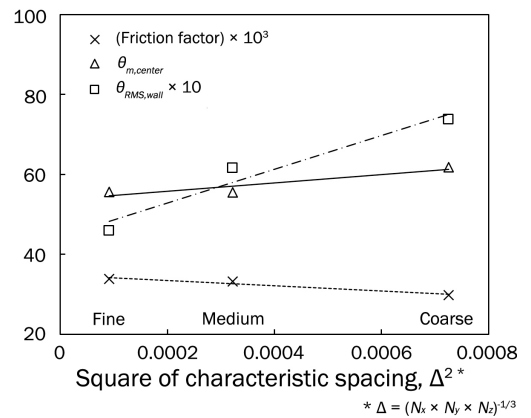| Grid type	Coarse	Medium	Fine	DNS [31, 32]
Friction factor	0.0298	0.0332	0.0339	0.0337
Error (%)	-11.76	-1.71	+0.58	-
$\theta_{m,center}$*	61.783	55.500	55.584	55.593
Error (%)	+10.41	-0.81	-0.66	-
$\theta_{RMS,wall}$*	7.372	6.157	4.595	4.473
Error (%)	-64.82	-37.66	-2.72	-

* Values are calculated under the condition of $C = 1, K = 1$

Fig. 5. Variation of physical properties with respect to the square of characteristic spacing defined as a cube-root of total number of cells

factors $\theta_{m,center}$ and $\theta_{RMS,wall}$ show nearly linear trends with respect to the square of the characteristic mesh spacing, which is defined as the cube-root of the total number of cells, as can be seen in Fig. 5. This verifies the second-order accuracy of the current numerical scheme.

Fig. 6 illustrates the mean streamwise velocity and temperature profiles along the wall-normal (*y*) direction. The velocity and temperature are normalized using the calculated friction velocity u_τ instead of U_b, and thus are expressed in a wall unit. Following Tiselj et al. [31], the fluid and solid phases have the same thermal diffusivity ($C \cdot K = 1$), indicating no scale difference in thermal diffusion between the two phases. Thus, for this case we used the scaling of the fluid phase for the solid region as well. All profiles agree well with theory and DNS data. The velocity profile closely follows the viscous sublayer and log-law profiles. The mean temperature gradient within the solid is smaller when the solid cell has larger thermal conductivity, since the heat flux *q* within the solid is constant. The mean temperature profile in the fluid region does not vary much with *C* and *K*, and follows the profile of the non-CHT data with

isothermal boundary condition. It can be seen that the type of thermal boundary condition has negligible influence on the fluid θ_m profiles for this case [34].

The RMS temperature, however, strongly depends on the thermal properties, as shown in Fig. 7. In the fluid region, the overall temperature fluctuations coincide fairly well with the reference DNS data for the different CHT coefficient conditions. They reach a peak just beyond the viscous sublayer, and then all decrease together toward the channel center. Towards the wall the profile approaches the constant heat flux
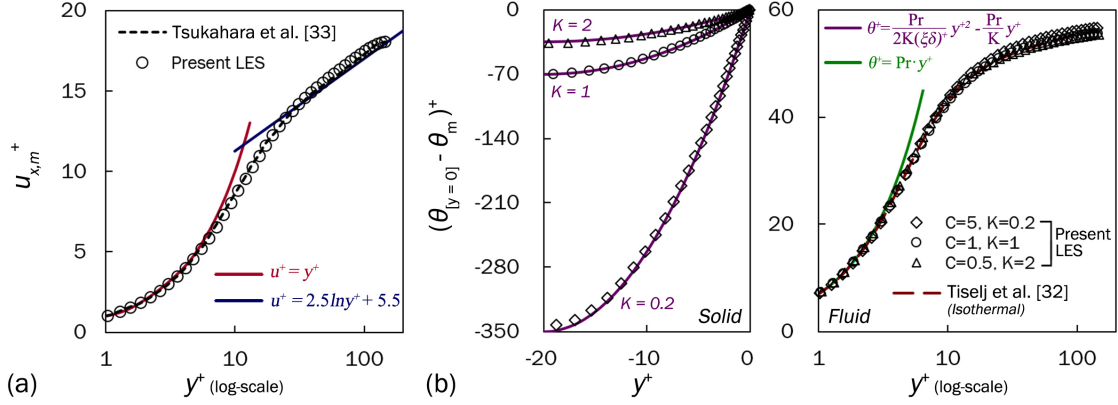
Fig. 6. Mean profiles of heated channel flow at $Re_\tau = 150$: (a) Fluid streamwise velocity; (b) Solid temperature (left) and fluid temperature (right)
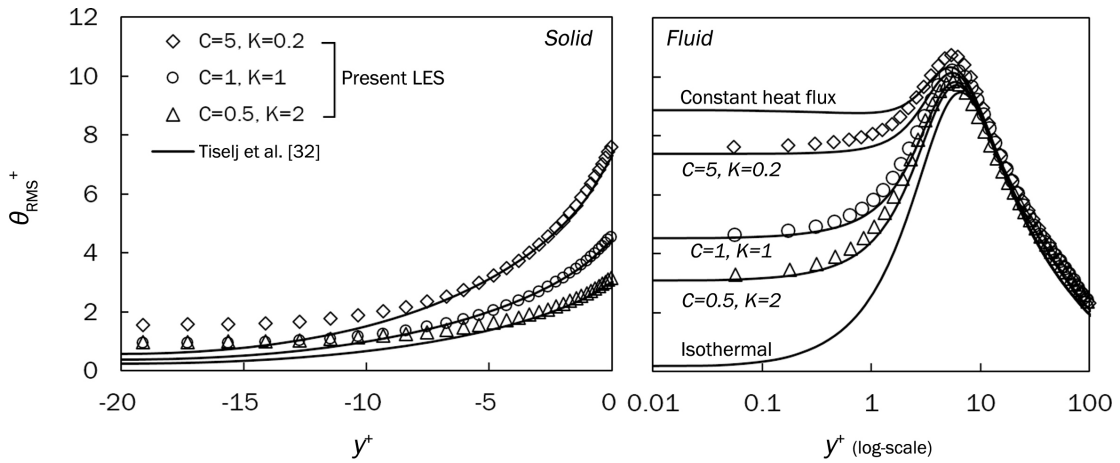

Fig. 7. Profiles of RMS temperature fluctuations of the heated channel flow at $Re_\tau = 150$ inside the solid slab (left) and in the fluid (right).

condition as C increases and K decreases, and the isothermal condition as C decreases and K increases. The θ_{RMS} difference between the DNS data at the wall does not exceed more than 6.2% for all the cases. In the solid region, a progressive decrease in θ_{RMS} appears as the distance from the solid-fluid interface increases. The data agree well with the reference DNS data for $-5 < y^+ < 0$ but display notable deviation beyond about $y^+ = -7$. This suggests that some oscillating components of θ originating from the interface did not damp out as they penetrated into the slabs during the simulation. Further experimental research might be required to resolve this issue because the energy equations in both LES and DNS are reduced to the identical heat conduction equation within the solid slab.

From the θ_{RMS} profiles in the fluid region, it can be inferred that the ideal isothermal boundary condition constitutes the lower limit of the CHT profile, whereas the ideal constant-heat-flux boundary condition serves as the upper limit of the CHT profile. This is because these two boundary conditions can be regarded as extreme cases of infinitely high $(\rho c_p)_s$ and k_s, and infinitely low $(\rho c_p)_s$ and k_s, respectively. Thus, the use of such ideal thermal boundary conditions might lead to an unrealistic approach.

3.2. Free convection in a closed square cavity

To test the ability of simulating thermally-driven flow, where the temperature acts as an active scalar, circulating flow due to temperature differences in vertical walls within a closed cavity (see Fig. 8) was analyzed. The geometry and relevant conditions of the cavity were based on the experiment of Tian and Karayiannis [35]. The reference length, velocity, and temperature for the nondimensionalization were chosen as the cavity height H, buoyancy velocity $\sqrt{g\beta H(T_h - T_c)}$ (where g is the gravitational acceleration and β is the thermal expansion coefficient), and the wall temperature difference $(T_h - T_c)$, respectively. Thus, Re in this case is equal to the square root of Gr. The grid parameters and material properties are summarized in Table 4. The validity of the grid system for LES was already confirmed by the numerical study of Zhang et al. [27], who researched the same problem but used a different numerical method.

For boundary conditions, a no-slip condition was applied at all solid-fluid interfaces, and constant temperature conditions of T_h and T_c were imposed at the hot wall $(x = 0)$ and cold wall $(x = H)$, respectively. The front wall, back wall, and the outer boundaries of the top and bottom walls were set as adiabatic. Unlike the other walls, the top and bottom walls were modeled by IB, and thus had volume to perform both non-CHT and CHT
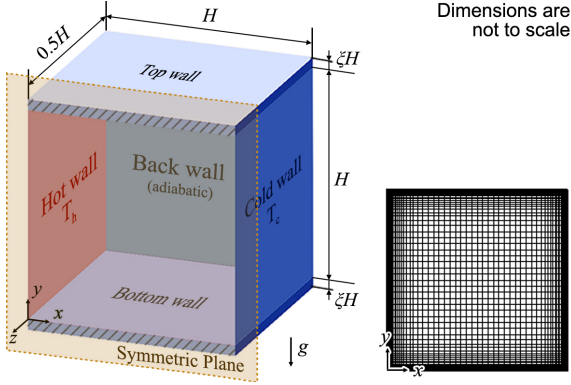
Fig. 8. (Left) geometry of flow in a closed square cavity and (right) grid system viewed at xy-plane.

Table 4
Grid parameters and material properties for channel flow

Domain size, $L_x \times L_y \times L_z$		$H \times (1 + 2\xi)H \times 2H$
Cell arrangement, $N_x \times N_y \times N_z$		$96 \times 128 \times 120$
Total number of cells		1,474,560
	$\Delta x/H$	0.0001 - 0.027
Grid interval	$\Delta y/H$	0.0001 - 0.027
	$\Delta z/H$	0.013 - 0.017
Number of cells inside the top or bottom wall in the y-direction		16
Volumetric heat capacity ratio, C		2.92×10^{-4}
Thermal conductivity ratio, K		1.88×10^{3}
Rayleigh number, $Ra(= Gr \cdot Pr)$		1.58×10^{9}
Prandtl number, Pr		0.71
Top & bottom wall thickness, ξ		0.002

analyses for comparison. In the non-CHT case, temperature distributions at the top and bottom walls were prescribed with experimentally measured profiles [27, 35], and only the fluid region was computed.

At the beginning, the flow is in a complete standstill with the uniform temperature of the median of T_h and T_c. Following Zhang et al. [27], turbulent statistics for the non-CHT case were obtained by averaging the data for the time interval between $90\sqrt{H/[g\beta(T_h - T_c)]}$ and $180\sqrt{H/[g\beta(T_h - T_c)]}$, because the circulation appeared to be quasi-stable within this interval. Subsequently, the CHT analysis was performed by changing C and K to realistic values, reflecting properties of air for fluid and mild steel for solid at nominal temperatures. To save computational time, the non-CHT field values at the time of $180\sqrt{H/[g\beta(T_h - T_c)]}$ were utilized as the initial condition for the CHT analysis. The simulation was then run for a time interval of $30\sqrt{H/[g\beta(T_h - T_c)]}$ for stabilization, and additionally carried out for the same interval for averaging.

Overall contours of the mean velocity and temperature fields near the top hot corner for the non-CHT and CHT cases are shown in Fig. 9, along with the experimental measurements of Tian and Karayiannis [35]. The results from both analyses show identical trends compared to the experimental reference data.
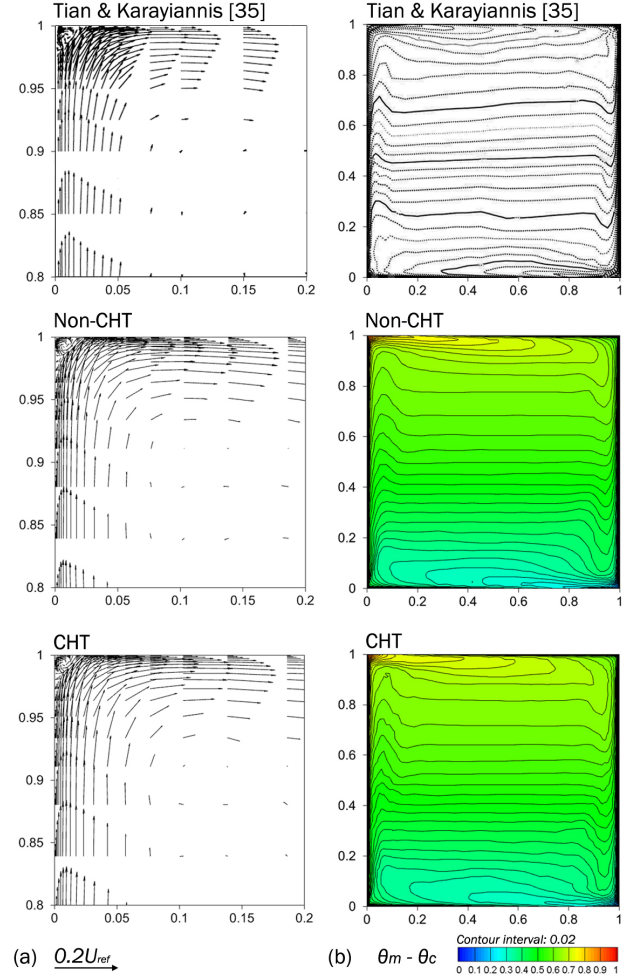

Fig. 9. (a) Mean velocity fields near the top hot corner and (b) overall mean temperature contours at the center of the cavity ($z = 0$). Horizontal and vertical axes correspond to x/H and y/H, respectively.

In the velocity field, a small separation bubble rotating counterclockwise is observed at the top hot corner, as well as the bottom cold corner. The length scale of the bubble is about 1% of the cavity height. In the temperature contour, the cores of thermal stratification are located close to the top hot corner and bottom cold corner. Additionally, the development of thermal boundary layers near the vertical walls can be seen via the contour lines.

For additional comparison of mean properties, in Fig. 10, the mean temperature and local Nusselt number (Nu) distributions along the bottom and top wall interfaces are plotted. Since the walls are thin, no significant thermal changes arise inside the wall. The formula of the local Nu is given as:

$$Nu_x = -\frac{H}{T_h - T_c} \left.\frac{\partial T}{\partial y}\right|_{y=0+ \text{ or } H-} \tag{11}$$

If its sign is negative, the direction of the corresponding heat flux is opposite to the axis direction. It is observed that the mean temperature at both the top and bottom horizontal walls changes abruptly near the vertical walls, whereas the change is gradual near the center (see Fig. 10a). The trends are similar
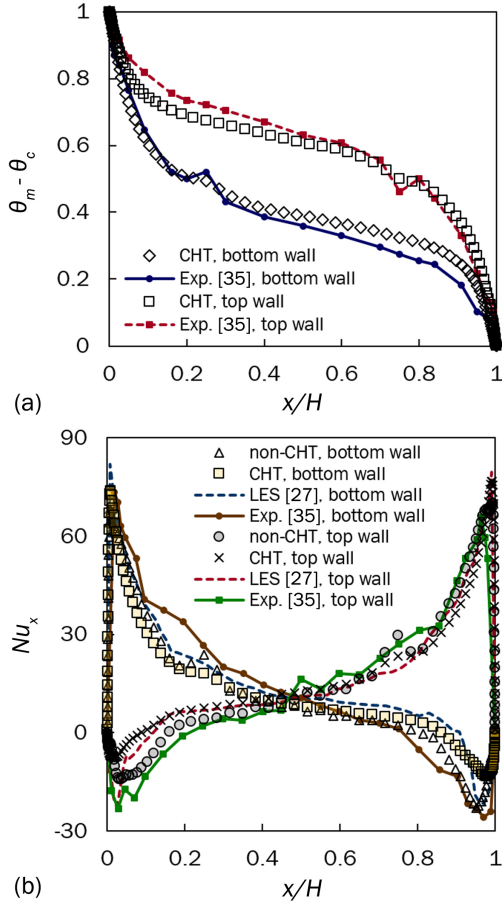
Fig. 10. (a) Mean temperature and (b) local Nusselt number distributions along the bottom ($y = 0$) and top ($y = H$) wall interfaces, compared with previous experimental and numerical results. All data are spatially averaged in the z direction.

Fig. 11. RMS temperature fluctuation profiles (a) at the mid-plane ($y = 0.5H$), and (b) at the bottom ($y = 0$) and top ($y = H$) wall interfaces at the center section ($z = 0$) of the cavity.

compared to the experimental data, but the temperature from the CHT cases shows steeper change at the corner, especially at the top near the hot vertical wall, and at the bottom near the cold vertical wall. Such steep change is likely to result in a local reduction of temperature difference between the fluid and solid, thus reducing the amount of local convective heat transfer. This can be confirmed in Fig. 10b, where the CHT case has a significantly lower absolute Nu_x value compared to the experimental or non-CHT cases, at $0.9 < x/H < 1$ for the bottom wall, and at $0 < x/H < 0.1$ for the top wall. One possible reason for this difference might be that the insulation of the horizontal walls was likely not perfect during the experiment, so that heat transfer might have occurred between the heated vertical plate and the top wall, and between the cooled vertical plate and the bottom wall. The non-CHT cases utilized the experimental temperature profiles, so had similar trends to the experiments.

The RMS temperature fluctuation profiles at the mid-plane ($y/H = 0.5$) and at the top and bottom walls in the center section ($z = 0$) are depicted in Fig. 11. Since meaningful fluctuations occur near both vertical walls in a symmetrical manner, the profiles are only shown near the hot wall. At the mid-plane, as shown in Fig. 11a, the CHT profile has no considerable dif-
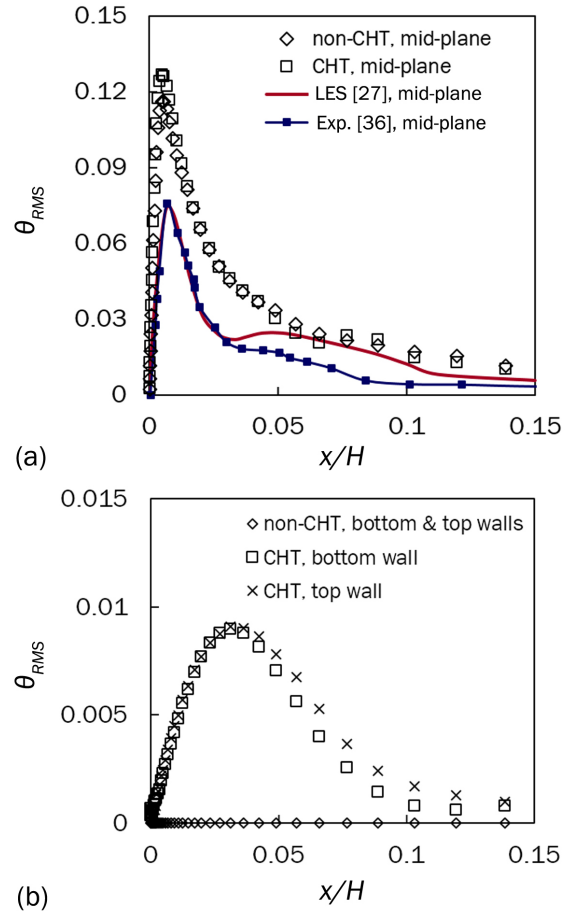
ference from the non-CHT profile. The present LES results overestimate the RMS values of the previous experimental and numerical data [27, 36], which means that the current combination of LES models cannot successfully resolve the turbulence near the wall for the current problem, possibly due to the oversimplification of the SGS heat flux model. On the other hand, Fig. 11b displays a stark difference between non-CHT and CHT analyses. Unlike non-CHT, non-zero θ_{RMS} values exist at the surface and inside the wall for CHT, with a maximum of about 0.009 at $x/H = 0.03$ for both walls. Therefore, the importance of CHT increases, especially when the near-wall region is of interest for heat transfer analysis.

3.3. Crossflow around a heated circular cylinder

External flow around a heated circular cylinder (see Fig. 12) was investigated as a curvilinear IB case, in which grid-interface discrepancy exists. The interpolation scheme, using the flood-fill algorithm with various levels of subdivision, was applied to find the optimal level. For validation, the simulation results were compared with the Nusselt number correlations of Hilpert [37] and Frossling [38], and the experimental data of Nakamura and Igarashi [39]. A constant volumetric heat source
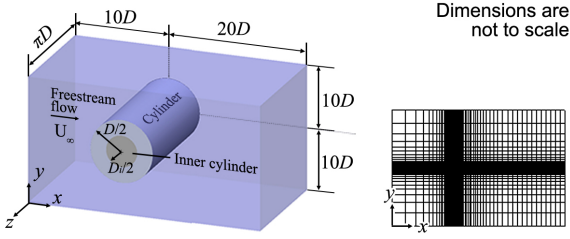
Fig. 12. (Left) geometry of crossflow around a circular cylinder and (right) grid system viewed at *xy*-plane.

Table 5
Grid parameters and material properties for crossflow

Domain size, $L_x \times L_y \times L_z$		$30D \times 20D \times \pi D$	
Grid type	Coarse	Medium	Fine
Cell arrangement, $N_x \times N_y \times N_z$	$96 \times 64 \times 32$	$192 \times 198 \times 32$	$288 \times 256 \times 32$
Total number of cells	196,608	768,432	2,359,296
	$\Delta x/D$	0.03 - 2.26	0.02 - 1.23	0.01 - 0.64
Grid interval $\Delta y/D$	0.03 - 2.26	0.02 - 1.23	0.01 - 0.64
$\Delta z/D$	0.10	0.10	0.10
Number of cells inside the cylinder in the $x-$ or $y-$ direction	32	64	128
Reynolds number, *Re*		400	
Prandtl number, *Pr*		0.71	
Volumetric heat capacity ratio, *C*		4.77×10^{-4}	
Thermal conductivity ratio, *K*		7.89×10^{3}	
Inner cylinder diameter, D_i		0.5D	

(q) is within the inner cylinder region. The reference length, velocity, and temperature for nondimensionalization were chosen as the cylinder diameter D, freestream velocity U_∞, and scaling temperature $Dq/[U_\infty(\rho c_p)_f]$, respectively. The grid parameters and material properties are listed in Table 5. The Reynolds number of 400 is known to be in the regime where the vortex street is fully turbulent [40]. The overall computational domain size was similar to that of the LES study of Taghinia et al. [41], who simulated a circular cylinder at a higher *Re* of 3,900. Natural convection was neglected ($Gr = 0$) for this problem.

For the streamwise (x) direction, Dirichlet boundary conditions, $u_x = 1, u_y = 0, u_z = 0$ and $\theta = \theta_\infty = 0$, were imposed at the inlet. Convective boundary conditions, $\partial u_i/\partial t^* + \bar{c}\partial u_i/\partial x^* = 0$ and $\partial\theta/\partial t^* + \bar{c}\partial\theta/\partial x^* = 0$, were prescribed at the outlet, where $\bar{c}$ is the spatial mean streamwise velocity at the exit plane. Farfield boundary conditions, $\partial u_x/\partial y^* = 0$, $u_y = 0$, $u_z = 0$, and $\partial\theta/\partial y^* = 0$, were used at the cross-stream (y) boundaries. A periodic boundary condition was imposed at the spanwise (z) boundaries. The cylinder was generated by the IB method, and thus satisfied the no-slip boundary condition.

For each simulation, turbulent statistics were obtained after the vortex street was fully generated and the solid temperature, which was initially the same as the freestream temperature, converged (meaning that its temporal change at the axis became less than 0.01% of the reference temperature per unit reference
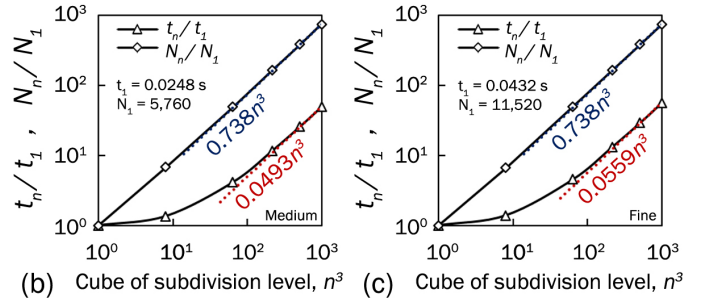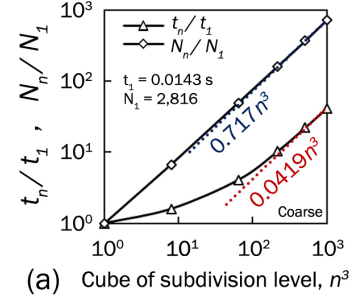

(a)   Cube of subdivision level, n^3

(b)   Cube of subdivision level, n^3 (c)   Cube of subdivision level, n^3

Fig. 13. CPU time consumed (t_n) and number of scanned sub-cells (N_n) during the flood-fill algorithm for interpolation, with respect to the subdivision level: (a) coarse grid, (b) medium grid, and (c) fine grid.

time scale D/U_∞). The time interval for averaging was set to $100D/U_\infty$, which was long enough to include nearly 20 cycles of vortex shedding, because the Strouhal number is about 0.2 for the current *Re* [40]. This was also confirmed after the simulations.

During grid interpolation, both computational time and accuracy of results are affected by not only the level of the subdivision, but also the grid quality of the solid-fluid interface. Hence, to optimize the subdivision level, we need to know whether it depends on the grid size or not. Thus, the subdivision test was conducted at six levels (1, 2, 4, 6, 8 and 10) for three different grids.

For the different grid systems, the trends of CPU time and number of scanned sub-cells during the interpolation scheme is shown in Fig. 13. It can be seen that the proportion of unidentified sub-cells reaches a consistent value of approximately 27%, regardless of the grid type. This is because the subdivision level becomes sufficient beyond 6, and the subdivided IBs become close to the actual solid-fluid interfaces. The current algorithm is thus expected to be 27% faster than the one-by-one method. The CPU time becomes linearly proportional to the cube of the subdivision level, but its sensitivity significantly increases as the grid quality increases.

Contours of mean streamwise velocity and temperature at *Re* = 400 are depicted in Fig. 14. To illustrate the differences, only the coarse and fine grid cases with subdivision levels of 1 and 10 are shown. The temperature is re-normalized by the spatial mean temperature at the cylinder surface ($\overline{T_s}$) via bilinear interpolation between grid points. Qualitatively, flow separation and recirculation are similarly observed in both grids, with a slightly wider wake for the fine grid case. The velocity field displays no difference between subdivision levels. The
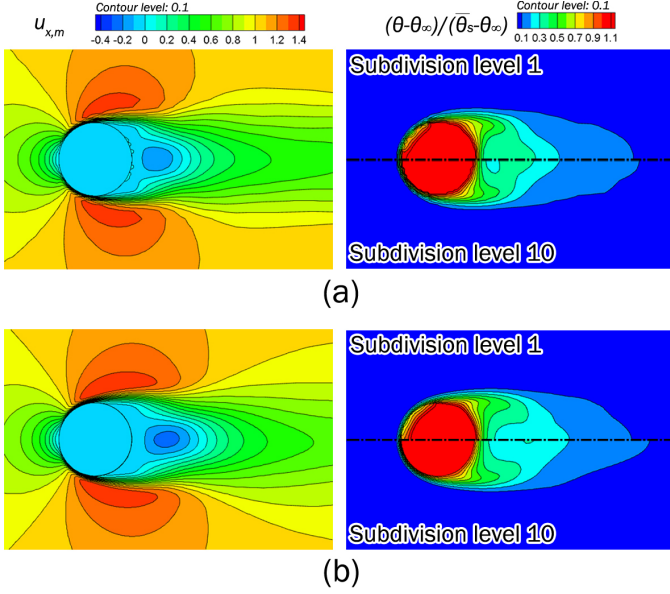
Fig. 14. Contours of (left) mean streamwise velocity and (right) mean temperature at $Re = 400$ with subdivision levels of 1 and 10, where $x \in [-1.25D, 3.25D]$ and $y \in [-1.5D, 1.5D]$: (a) coarse grid and (b) fine grid.

Fig. 15. Nu_D for the cylinder at $Re = 400$, compared to Hilpert's empirical value of 9.940 [37].

Fig. 16. Nu_ϕ distribution over a circular cylinder at $Re = 400$, compared to the correlation prior to flow separation and experimental data at the rear stagnation point.

temperature in this case is a passive scalar, thus it has no effect on the velocity field. In the case of the temperature contour, however, a low subdivision level results in poor temperature prediction within the cylinder, as observed at the front part of the cylinder. Since the thermal conductivity of the solid is considerably high, the Biot number of the solid is much less than 1. Thus, the temperature distribution within the cylinder should be nearly uniform, similar to the subdivision level 10 contour.

For quantitative analysis, the overall mean Nusselt number for the cylinder (Nu_D) is presented and compared with the empirical value in Fig. 15. The Nu_D is calculated from the angular average of the local Nu_ϕ at the cylinder surface, which is given as

$$ Nu_\phi = -\frac{D}{T_s - T_\infty} \left.\frac{\partial T}{\partial r}\right|_{r=0.5D+} \qquad (12) $$

where r is the distance from the cylinder axis and ϕ is the angle from the front stagnation point. The Nu_D calculated from the fine grid with a subdivision level of 6 shows only 0.16% absolute error compared to Hilpert's correlation [37]. Although the accuracy increases with grid quality, the convergence trend with respect to the subdivision level is similar between the different grids. As can be seen, after the level exceeds 6, the proportion of unidentified sub-cells converge, and the Nu_D does not change very much. Since the algorithm's calculation time proportionally increases with the cube of the subdivision level as indicated in Fig. 13, the subdivision level of 6 can be considered optimal to achieve both accuracy and efficiency for this simulation. It is suggested that the optimal subdivision level, in general, should be the level at which the overall proportion of unidentified sub-cells converges to a consistent value (which will vary with respect to the predetermined geometry).

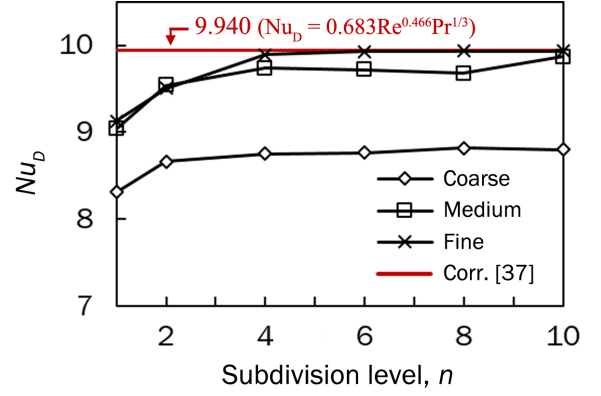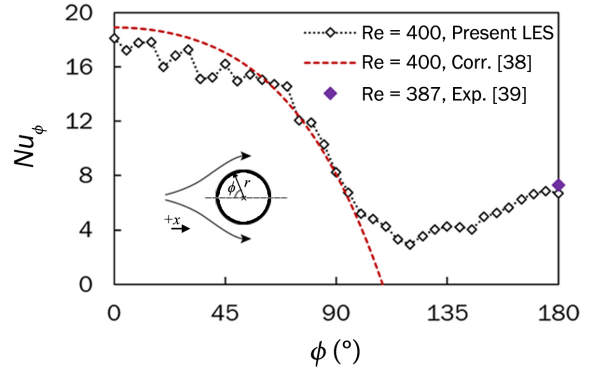Fig. 16 shows the distribution of Nu_ϕ along the cylinder sur-

face with a subdivision level of 6 for the fine grid system. Small oscillations of the data for small ϕ are mainly due to the discrepancy between the grid and interface. A refined approach that does not use the current simple bilinear interpolation might reduce this, but the present data nevertheless agree well with Frossling's correlation at $Re = 400$ [38], before flow separation occurs near $\phi = 90°$. After entering the turbulent wake region, the Nu_ϕ rises due to mixing. At the rear stagnation point ($\phi = 180°$), the LES value coincides with the measured experimental value of 7.3 [39] within 7.9%.

4. Conclusion

In the present study, a numerical method for conjugate heat transfer analysis was developed, to simulate both heat conduction in solid and heat convection in fluid regimes simultaneously. An immersed boundary method was utilized to generate the solid geometry in the computational domain, where the no-slip boundary condition was imposed. Two subgrid-scale models for turbulent stress and heat flux were implemented into the solver for large eddy simulation (LES). In order to interpolate thermal properties such as volumetric heat capacity and thermal conductivity at the solid-fluid interface, an efficient inter-

polation scheme based on the flood-fill algorithm was devised and applied. The performance of the interpolation depended on the subdivision level of the interface cells to identify the cells' configuration (between solid and fluid).

For validation, three different conjugate-heat-transfer problems containing turbulent flow were simulated using the present method: 1) channel flow between heated slabs, 2) thermally-driven flow in a closed cavity, and 3) crossflow around a heated circular cylinder. Overall, the results coincided well with those of the previous studies. However, notable overestimation of the temperature fluctuation for the second case, where the temperature acts as an active scalar, suggests that a more sophisticated model for the subgrid-scale heat flux might be needed for such thermally-driven flow. Nevertheless, the current conjugate-heat-transfer method predicted fairly accurately the thermal characteristics resulting from the interaction between the two phases, which cannot be estimated by conventional methods using isothermal or constant-heat-flux boundary conditions. Finally, the performance of the interpolation scheme was tested, and the trade-off between computational time and accuracy was examined. A subdivision level of 6 seems to be an optimal level for the current analysis.

Acknowledgements

References

[1] A. A. Ameri, R. Bunker, Heat Transfer and Flow on the First Stage Blade Tip of a Power Generation Gas Turbine: Part 2 - Simulation Results, in: ASME 1999 International Gas Turbine and Aeroengine Congress and Exhibition, American Society of Mechanical Engineers, 1999, pp. V003T01A086–V003T01A086.

[2] H. Yang, S. Acharya, S. V. Ekkad, C. Prakash, R. Bunker, Numerical Simulation of Flow and Heat Transfer past a Turbine Blade with a Squealer-Tip, in: ASME Turbo Expo 2002: Power for Land, Sea, and Air, American Society of Mechanical Engineers, 2002, pp. 295–307.

[3] J.-Y. Jang, L.-K. Chen, Numerical Analysis of Heat Transfer and Fluid Flow in a Three-Dimensional Wavy-Fin and Tube Heat Exchanger, International Journal of Heat and Mass Transfer 40 (16) (1997) 3981–3990.

[4] T. J. Rennie, V. G. Raghavan, Numerical Studies of a Double-Pipe Helical Heat Exchanger, Applied Thermal Engineering 26 (11-12) (2006) 1266–1273.

[5] L. L. Castro, A. Aranda, G. Urquiza, Analysis of Heat Transfer in an Experimental Heat Exchanger Using Numerical Simulation, InTech, 2016.

[6] J. Jayakumar, S. Mahajani, J. Mandal, P. Vijayan, R. Bhoi, Experimental and CFD Estimation of Heat Transfer in Helically Coiled Heat Exchangers, Chemical Engineering Research and Design 86 (3) (2008) 221–232.

[7] Z. Zhang, D. Ma, X. Fang, X. Gao, Experimental and Numerical Heat Transfer in a Helically Baffled Heat Exchanger Combined with One Three-Dimensional Finned Tube, Chemical Engineering and Processing: Process Intensification 47 (9-10) (2008) 1738–1743.

[8] H. Zeng, N. Diao, Z. Fang, Heat Transfer Analysis of Boreholes in Vertical Ground Heat Exchangers, International Journal of Heat and Mass Transfer 46 (23) (2003) 4467–4481.

[9] D. Bohn, J. Ren, K. Kusterer, Conjugate Heat Transfer Analysis for Film Cooling Configurations with Different Hole Geometries, in: ASME Turbo Expo 2003, collocated with the 2003 International Joint Power Generation Conference, American Society of Mechanical Engineers, 2003, pp. 247–256.

[10] B. W. Webb, S. Ramadhyani, Conjugate Heat Transfer in a Channel with Staggered Ribs, International Journal of Heat and Mass Transfer 28 (9) (1985) 1679–1687.

[11] Y. Oda, K. Takeishi, Y. Miyake, Numerical Study of Conjugate Heat Transfer in Pin-Fin Channels Based on Large-Eddy Simulation Data, Computational Thermal Sciences: An International Journal 4 (3).

[12] M. Wang, J. G. Georgiadis, Parallel Computation of Forced Convection Using Domain Decomposition, Numerical Heat Transfer, Part B: Fundamentals 20 (1) (1991) 41–59.

[13] M. Wang, J. G. Georgiadis, Conjugate Forced Convection in Crossflow over a Cylinder Array with Volumetric Heating, International Journal of Heat and Mass Transfer 39 (7) (1996) 1351–1361.

[14] W. Qu, I. Mudawar, Experimental and Numerical Study of Pressure Drop and Heat Transfer in a Single-Phase Micro-Channel Heat Sink, International Journal of Heat and Mass Transfer 45 (12) (2002) 2549–2565.

[15] S. V. Patankar, Numerical Heat Transfer and Fluid Flow, Washington, DC, Hemisphere Publishing Corp.

[16] G. Iaccarino, S. Moreau, Natural and Forced Conjugate Heat Transfer in Complex Geometries on Cartesian Adapted Grids, Journal of Fluids Engineering 128 (4) (2006) 838–846.

[17] K. Nagendra, D. K. Tafti, K. Viswanath, A New Approach for Conjugate Heat Transfer Problems Using Immersed Boundary Method for Curvilinear Grid Based Solvers, Journal of Computational Physics 267 (2014) 225–246.

[18] J. C. Song, J. Ahn, J. S. Lee, An Immersed-Boundary Method for Conjugate Heat Transfer Analysis, Journal of Mechanical Science and Technology 31 (5) (2017) 2287–2294.

[19] A. Pilkington, B. Rosic, S. Horie, Methods for Controlling Gas Turbine Casing Flows During Engine Shutdown, International Journal of Turbomachinery, Propulsion and Power 3 (2) (2018) 17.

[20] N. Park, S. Lee, J. Lee, H. Choi, A Dynamic Subgrid-Scale Eddy Viscosity Model with a Global Model Coefficient, Physics of Fluids 18 (12) (2006) 125109.

[21] J. Smagorinsky, General Circulation Experiments with the Primitive Equations: I. The Basic Experiment, Monthly Weather Review 91 (3) (1963) 99–164.

[22] A. Vreman, An Eddy-Viscosity Subgrid-Scale Model for Turbulent Shear Flow: Algebraic Theory and Applications, Physics of Fluids 16 (10) (2004) 3670–3681.

[23] P. Moin, K. Squires, W. Cabot, S. Lee, A Dynamic Subgrid-Scale Model for Compressible Turbulence and Scalar Transport, Physics of Fluids A: Fluid Dynamics 3 (11) (1991) 2746–2757.

[24] B.-C. Wang, E. Yee, D. J. Bergstrom, O. Iida, New Dynamic Subgrid-Scale Heat Flux Models for Large-Eddy Simulation of Thermal Convection Based on the General Gradient Diffusion Hypothesis, Journal of Fluid Mechanics 604 (2008) 125–163.

[25] A.-S. Yang, C.-C. Chieng, Turbulent Heat and Momentum Transports in an Infinite Rod Array, Journal of Heat Transfer 109 (3) (1987) 599–605.

[26] B. G. Huh, S. Kim, C. H. Chung, The Turbulent Prandtl Number for Temperature Analysis in Rod Bundle Subchannels, Journal of Nuclear Science and Technology 42 (2) (2005) 183–190.

[27] Z. Zhang, W. Chen, Z. Zhu, Y. Li, Numerical Exploration of Turbulent Air Natural-Convection in a Differentially Heated Square Cavity at Ra = 5.33×10^9, Heat and Mass Transfer 50 (12) (2014) 1737–1749.

[28] J. Kim, D. Kim, H. Choi, An Immersed-Boundary Finite-Volume Method for Simulations of Flow in Complex Geometries, Journal of Computational Physics 171 (1) (2001) 132–150.

[29] J. Kim, H. Choi, An Immersed-Boundary Finite-Volume Method for Simulation of Heat Transfer in Complex Geometries, KSME International Journal 18 (6) (2004) 1026–1035.

[30] D. K. Lilly, A Proposed Modification of the Germano Subgrid-Scale Closure Method, Physics of Fluids A: Fluid Dynamics 4 (3) (1992) 633–635.

[31] I. Tiselj, R. Bergant, B. Mavko, I. Bajsic, G. Hetsroni, DNS of Turbulent

11

Heat Transfer in Channel Flow with Heat Conduction in the Solid Wall, Journal of Heat Transfer 123 (5) (2001) 849–857.

[32] T. Tsukahara, Y. Seki, H. Kawamura, D. Tochio, DNS of Turbulent Channel Flow at Very Low Reynolds Numbers, in: TSFP Digital Library Online, Begel House Inc., 2005, pp. 935–940.

[33] H. Kawamura, K. Ohsaka, H. Abe, K. Yamamoto, DNS of Turbulent Heat Transfer in Channel Flow with Low to Medium-High Prandtl Number Fluid, International Journal of Heat and Fluid Flow 19 (5) (1998) 482–491.

[34] I. Tiselj, L. Cizelj, DNS of Turbulent Channel Flow with Conjugate Heat Transfer at Prandtl Number 0.01, Nuclear Engineering and Design 253 (2012) 153–160.

[35] Y. Tian, T. Karayiannis, Low Turbulence Natural Convection in an Air Filled Square Cavity: Part I: The Thermal and Fluid Flow Fields, International Journal of Heat and Mass Transfer 43 (6) (2000) 849–866.

[36] Y. Tian, T. Karayiannis, Low Turbulence Natural Convection in an Air Filled Square C: Part II: The Turbulence Quantities, International Journal of Heat and Mass Transfer 43 (6) (2000) 867–884.

[37] R. Hilpert, Heat Transfer from Cylinders, Forsch. Geb. Ingenieurwes 4 (1933) 215.

[38] N. Frössling, Evaporation, Heat Transfer, and Velocity Distribution in Two-Dimensional and Rotationally Symmetrical Laminar Boundary-Layer Flow, Report, National Aeronautics and Space Admin Langley Research Center Hampton VA (1956).

[39] H. Nakamura, T. Igarashi, Unsteady Heat Transfer from a Circular Cylinder for Reynolds Numbers from 3000 to 15,000, International Journal of Heat and Fluid Flow 25 (5) (2004) 741–748.

[40] J. H. Lienhard, Synopsis of Lift, Drag, and Vortex Frequency Data for Rigid Circular Cylinders, Vol. 300, Technical Extension Service, Washington State University, 1966.

[41] J. Taghinia, M. M. Rahman, T. Siikonen, Large Eddy Simulation of Flow past a Circular Cylinder with a Novel Sub-Grid Scale Model, European Journal of Mechanics-B/Fluids 52 (2015) 11–18.